High Temperature Corrosion of Materials (2025) 102:19
https://doi.org/10.1007/s11085-025-10339-1

RESEARCH

Comparison of Laboratory-Scale Methods for Assessing Deposit-Induced Corrosion of Boiler Materials in Biomass Combustion and Recovery Boilers

J.-E. Eriksson[1] · S. Mori[2] · L. Silvander[1] · L. Hupa[1] · J. Lehmusto[1]

Received: 6 March 2025 / Revised: 4 June 2025 / Accepted: 6 June 2025
© The Author(s) 2025

Abstract

Various instrumental methods for analyzing high-temperature corrosion of boiler materials were explored and compared. These methods were applied to gain deeper insights into corrosion due to two salt mixtures containing Na, K, SO_4, and Cl below and above the mixtures' first melting points. Stainless steel AISI316 and high-alloyed Sanicro28, typically used in heat exchangers in power plants, were exposed to salt mixtures in a laboratory tube furnace for 168 h. The extent of the metal corrosion following exposure was measured through mass loss, changes in the surface topography using optical 3D imaging, and dimensional metrology. Additionally, the morphology, thickness, and composition of the formed oxide scales were characterized using SEM–EDX. The information gathered from each method confirmed the impact of the synthetic salt deposit and temperature on the metal corrosion. Combining several methods enables detailed studies of changes taking place on the metal surface after exposure to challenging environments. The results also suggested that partial melting of the deposit had a higher impact on the corrosion than its chloride content.

Keywords High-temperature corrosion · Corrosion analysis · First melt temperature

Introduction

The corrosion rate of steels and alloys in power plants is critical for their maximum steam temperature and efficiency. The maximum achievable steam temperature largely depends on the chemical composition of the fuel, which determines

✉ J.-E. Eriksson
jan-erik.eriksson@abo.fi

[1] Johan Gadolin Process Chemistry Centre, Åbo Akademi University, Turku, Finland

[2] Faculty of Engineering and Applied Science, Centre for Energy Engineering, Cranfield University, Cranfield, UK

Published online: 26 June 2025

the flue gas environment. While coal- and gas-fired boilers can operate at steam temperatures above 600 °C, lower-grade fuels, such as biomass and waste, typically have a maximum steam temperature of around 500 °C [1]. This limitation is due to the higher content of corrosive species (e.g., Cl and S) in biomass and waste, which are released during combustion as alkali vapors. These vapors can condense and interact or stick to heat transfer surfaces, causing material degradation, especially if some molten fraction is present in the deposit. The extent of this corrosion depends on the surface temperature of the heat exchanger material and the chemical composition of the deposit.

Efforts to achieve more sustainable energy production continue to drive interest in biomass and other waste-derived fuels [2]. Biomass, such as forest and agricultural residues, is often considered a CO_2-neutral fuel because the amount of CO_2 absorbed during biomass growth through photosynthesis is roughly equal to the CO_2 released during combustion. However, power plants using biomass and waste-derived fuels must achieve similar or close steam temperatures to serve as a viable alternative to fossil fuels. Generally, increasing the steam temperature by 10 °C boosts power production efficiency by approximately 2% [3, 4].

As a result of ash composition being so different from coal-fired plants, power plants using biomass or waste as fuel have been compelled to operate at lower steam temperatures to mitigate corrosion, compromising power production efficiency. Consequently, effective corrosion prevention strategies are essential for these plants to operate at higher steam temperatures. Preventing corrosion involves careful material selection, as well as regular inspection and maintenance, all of which come with associated costs. Understanding detailed chemistry and the impact of melt formation in deposits is relevant. For these reasons, reliable methods for detecting and predicting corrosion are essential. Various well-known methods are available to identify and measure corrosion. Some methods focus on studying corrosion mechanisms, while others compare the relative corrosion of different alloys in these conditions. Accurate and reliable analytical laboratory-scale techniques are crucial for assessing the relative degradation rates and mechanisms of materials exposed to high temperatures in corrosive environments. Research on corrosion typically involves laboratory-scale furnace tests using steel coupons with synthetic or real ash deposits. Additionally, probe measurements can be taken by exposing steel samples inside operating boilers, and damage analysis can be conducted after the boiler shutdown [5]. After exposure, test samples or boiler components are analyzed in the laboratory, often using techniques such as scanning electron microscopy or other advanced methods. Standard analytical tools and techniques for examining boiler materials exposed to high-temperature corrosive environments in laboratory scale include various methods, e.g., [6]

1. Weight Loss Measurements, where the mass of a sample is measured before and after exposure to a corrosive, high-temperature environment. The weight loss indicates the extent of corrosion that has occurred. In some cases, weight gain is used to measure the amount of oxide formed. The technique helps compare the corrosion of steel samples over a specific period, thereby aiding in the selection of

materials. Weight loss measurements are also straightforward and cost-effective. The limitation is that this method provides no information on the corrosion products or mechanisms.

2. Scanning Electron Microscopy (SEM) is often used to examine the surface morphology of the corroded sample at high magnification. It can reveal surface features, such as cracks, pits, degradation, and oxidation. It provides detailed imaging, but as a limitation, it requires sample preparation and can be time-consuming and costly. SEM is often equipped with X-ray spectroscopy.
3. Energy-Dispersive X-ray Spectroscopy (EDX) is often used with SEM to identify the elemental composition of corrosion products and deposits. A limitation is that it fails to detect small concentrations (< 1000 ppm) and identify light elements.
4. Surface Profilometry measures surface morphology, e.g., changes in surface topography due to corrosion, depth of corrosion pits, or damage. The technique is typically applied to metal surfaces after removing the oxide layer. It can be integrated with weight change measurements and microscopy and is typically easy to use. However, similar to weight change measurements and microscopy, it only provides information about morphology and does not reveal the chemical nature of corrosion.
5. Dimensional Metrology (DM) measures the extent of changes in the metal samples by comparing pre- and post-exposure sample thickness. This method allows for creating probability plots describing the degree of metal regression and internal damage [7–9]. One advantage of DM is that it requires no corrosion scale removal. Thus, the same sample provides both corrosion quantification and corrosion product identification. However, it is important to note that the method requires using symmetrical samples with simple cross-sectional shapes (e.g., circles, squares, rectangles) [8].

Other techniques, such as Electron Probe Microanalysis, X-ray Photoelectron Spectroscopy, Fourier Transform Infrared Spectroscopy, and X-ray Diffraction, have been used to identify corrosion of boiler materials [6]. However, as these methods were not applied in the present study, they are not discussed further.

The techniques used in this work are generally employed to gain an enhanced understanding of high-temperature corrosion, including its rate, the composition of corrosion products, and the underlying mechanisms. These methods are effective for comparing different steels under specified idealized conditions. The selection of the method depends on the specific information required, the material under investigation, and the resources available.

When comparing various methods for assessing deposit-induced corrosion, two salts with different ratios of potassium (K) and chlorine (Cl) added in a non-corrosive K_2SO_4-Na_2SO_4 mixture were utilized. In a previous study, this sulfate mixture was non-corrosive under similar test conditions [10]. The calculated first melting temperature of this binary system is also well above our test temperatures (¨830 °C).

It was assumed that these two salts would also enable exploring details of the impact of the share of K and Cl in the sulfate deposit on the metal corrosion at temperatures close to the salts' first melting point.

The primary objective of this study was to investigate the challenges and benefits of various laboratory-scale methods for analyzing and measuring high-temperature corrosion induced by synthetic deposits. Well-established techniques were further developed and compared with newer methods to assess their capabilities, advantages, and disadvantages, ultimately assisting in selecting the most suitable method for specific cases. Additionally, the salt compositions and exposure conditions were chosen to provide detailed insights into the effects of potassium and chlorine in a sulfate deposit on the corrosion of boiler materials.

Experimental Procedures

Alloys

The heat transfer materials exposed to typical deposits for biomass combustion were commercial austenitic stainless steels AISI316 and Sanicro28. The elemental compositions of the steels were analyzed with SEM–EDX (Table 1).

For every furnace exposure, three coupons measuring 20×20×5 mm were cut from both alloys. The top surface of each coupon was polished with SiC papers, starting with grits 120–360, as described by Skrifvars et al. [11, 12]. The final polishing was completed using grit 500 SiC paper and ethanol. After drying, the average mass of the coupons was determined. Two coupons from each alloy and exposure condition were weighed three times using a Mettler XS105 scale (accuracy 0.01 mg), and the average value was recorded. The coupons were also imaged with a Bruker Alicona optical 3D profilometer before exposure.

Deposits

Synthetic ash deposits mimicking deposits in kraft recovery boilers were prepared by weighing and mixing Na_2SO_4, K_2SO_4, NaCl, and KCl [13]. After melting, the mixtures were ground to a homogenous synthetic deposit [13]. This process ensured that any local variations in the chemical composition of the deposits after the furnace exposures could be attributed to temperature gradients rather than being a result of an initially inhomogeneous deposit. The ground particles were sieved to a particle size range of 53 and 250 µm. The deposits were labeled

Table 1 EDX analysis (wt%) of the heat-transfer materials

	Fe	Cr	Mo	Mn	Si	Ni	C
AISI316	66.1	17.1	2.1	1.9	0.8	12.0	
Sanicro28	36.1	27.4	3.5	1.1	0.5	31.4	0.01

Only the main components were considered.

Table 2 Nominal and measured compositions, the first melting temperature T_0, and melt fraction of synthetic ash deposits at the studied temperatures

Synthetic ash		Na [wt-%]	K [wt-%]	Cl [wt-%]	SO_4 [wt-%]	T_0 [°C]	Melt fraction 500 °C [%]	Melt fraction 575 °C [%]
10K1Cl	Nominal	25	10	1	64	540	0	5.9
	measured	28	7	2	64	556	0	9.6
1K10Cl	Nominal	33	1	10	56	609	0	0
	measured	33	1	11	55	613	0	0

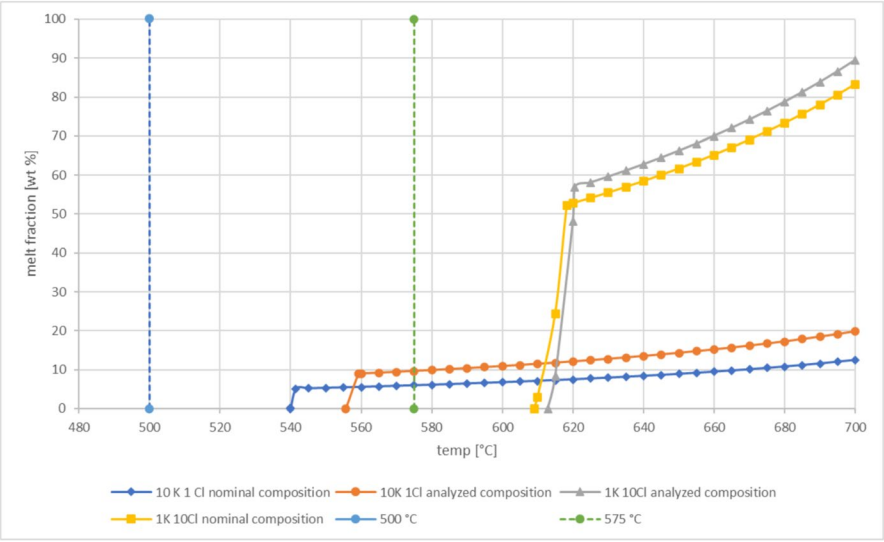


Fig. 1 Calculated (FactSage 8.1) melt fractions of 10K1Cl and 1K10Cl deposits using nominal and analyzed compositions. The vertical lines indicate the temperatures during the furnace exposures

as 10K1Cl and 1K10Cl based on the nominal mass ratio of potassium to chlorine. The final deposit compositions were analyzed using SEM–EDX (Table 2). The table also shows the nominal salt composition. These analyzed compositions were used to calculate the first melting temperature and its corresponding amount of molten phase for both salts with thermodynamic modeling using FactSage 8.1 (Fig. 1). The first melting temperature of 1K10Cl was markedly higher than the exposure temperatures. In contrast, around 10 wt% melt forms in 10K1Cl when exposed to 575 °C. This amount can be higher if metal halides are formed during corrosion [10].

Deposit Exposures

The corrosion experiments using both salt mixtures were carried out at 500 and 575 °C (Fig. 1). Three coupons of both alloys, two with the deposit and one reference without the deposit, were simultaneously exposed for each experimental condition (deposit and temperature) in a horizontal Carbolite tube furnace equipped with an inner alumina tube. A gas-tight quartz tube with gas inlets and outlets was inserted inside the alumina tube (Fig. 2). This setup enabled controlled atmospheres in the tube reactor. All experiments used an airflow rate of 0.2 l/min (0.17 cm/s) at NTP (building air).

Before the furnace exposures, 0.25 g of deposit was placed on the top surface of the coupons using a mold (diam. 15 mm, total deposit volume ~ 900 mm^3). The coupons were inserted into the furnace on a sample holder at room temperature. Then, the furnace was heated at a rate of 8 °C/min in an N_2 flow of 0.5 l/min, to ensure an inert atmosphere before reaching the target temperature. Once the target temperature was reached, nitrogen was replaced by an airflow (compressed building air, available in the gas lines in our laboratory) of 0.2 l/min (0.17 cm/s). The exposure time at the target temperature was 168 h, after which the furnace was shut off and cooled to room temperature in an N_2 flow of 0.5 l/min. During the exposures, the temperature was monitored with thermocouples attached to the sample holder, and samples were maintained within ± 2 °C of the target temperature.

Sample Treatment

After each furnace exposure, one coupon with a deposit was studied for material loss through gravimetry and optical 3D topography measurements, while the other one with a deposit was studied using SEM–EDX and DM.

The salt deposit and oxide scale were removed from the coupon before the mass loss determination. The coupon was washed in 20 ml reverse osmosis water using an ultrasound bath (Fisherbrand FB11201) for 180 s. Then, the coupon was dried and rewashed in 20 ml 1 M HCl in the ultrasound bath for another 180 s. Finally, the coupons were rinsed with distilled water and dried. After drying in a desiccator for 24 h, the coupons were weighed three times. Then, the area with visible signs of corrosion was defined from photographs of each surface. The changes in mass and the corroded area were used to calculate the material loss per unit area (mg/cm^2), assuming corrosion was uniform along the visibly attacked area. The volume of the

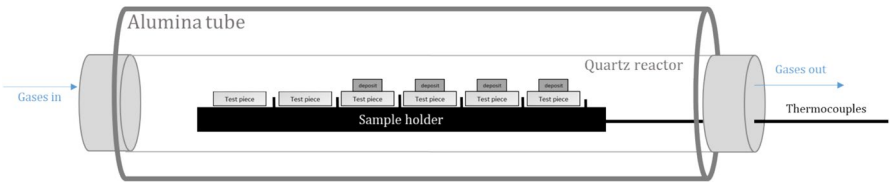


Fig. 2 Schematics of the quartz reactor used in experiments

removed material was based on the measured mass loss and the density (8.0 g/cm^3) of the alloy. This volume was then used to calculate the average thinning (µm) for the attacked surface area (Table 3). The etching process was verified by testing an exposed reference sample with no deposit. No mass loss was measured. The measured and calculated mass change and metal thinning after the deposit and furnace exposures are presented in Table 3.

Before SEM–EDX and DM analyses, the deposit was fixed with a small amount of epoxy resin and allowed to harden overnight. The coupon was cast in a chlorine-free epoxy resin and cured for 12 h. After curing, the epoxy-embedded coupon was cut with a precision saw to expose the cross-sectional surface. The other half was prepared for SEM analysis, while the counterpart was used for DM measurements (Cranfield University). The cross-sectional surface was polished and carbon-coated for SEM imaging and EDX analyses (SEM–EDX, Leo 1530 Gemini, Thermon Scientific UltraDry SDD X-ray detector).

Instrumental Methods for Analyzing Corrosion

Oxide Scale Thickness

The thickness of the corrosion oxide layer was measured from SEM Backscatter images using a novel in-house software developed for this purpose. This new software employs grayscale to color the oxide layer, enabling rapid thickness measurements even for a complex multi-layered oxide scale. The corrosion layer can be colored in minutes by adjusting the image characteristics to distinguish the oxide scale from the underlying metal and any deposit. This technique enables rapid processing of single or panorama Back Scattering SEM images. The oxide scale is represented in color based on a selected grayscale range, with green chosen for

Table 3 Measured and calculated data of AISI316 and Sanicro28 after exposure to synthetic deposits containing potassium and chlorine in a laboratory furnace at 500 and 575 °C

Deposit	Temp	Alloy	Gravimetry and visual inspection				3D Topography	
			Visible corrosion area	Measured loss	Calculated loss/area	Calculated thinning	Measured volume loss	Calculated thinning
	[°C]		[cm^2]	[mg]	[mg/cm^2]	[µm]	[mm^3]	[µm]
10K1Cl	500	AISI316	*2.5*	*− 1.7*	*− 0.7*	*− 0.9*	*− 0.25*	*− 0.6*
		Sanicro28	Nd	Nd	Nd	Nd	− 0.20	− 0.5
	575	AISI316	6.6	− 134.8	− 20.4	− 25.5	− 10.40	− 25.9
		Sanicro28	4.2	− 49.4	− 11.7	− 14.6	− 7.09	− 16.9
1K10Cl	500	AISI316	*3.8*	*− 1.4*	*− 0.4*	*− 0.5*	*− 0.18*	*− 0.4*
		Sanicro28	Nd	Nd	Nd	Nd	− 0.16	− 0.4
	575	AISI316	4.2	− 6.7	− 1.6	− 2.0	− 0.76	− 1.8
		Sanicro28	*4.2*	*− 1.0*	*− 0.2*	*− 0.3*	*− 0.42*	*− 1.0*

Italic values indicate low measured values, and n.d. indicates not detected.

visualization in this work. The software permits the user to select specific image areas, such as multiple lines, slices, or the entire image. Then, the software automatically calculates the thickness of the green-colored scale across the selected regions. Consequently, the colored images clearly differentiate the oxide scale, enabling the measurement of thickness data in terms of the corrosion layer mean thicknesses and standard deviation.

Surface Topography

The coupons' topography was measured before and after the high-temperature exposures using Bruker Alicona InfiniteFocus G6 optical 3D measuring device, operated through Bruker Laboratory Measurement Module software. 800WD17 lens was utilized to capture a total of 16 × 16 images of each coupon's surface, covering an area of 22.8 × 22.8 mm. The vertical and lateral resolutions were set to 750 nm and 3.13 µm, respectively. After imaging, Bruker MetMax software was used to align the images taken before and after exposure and to process the data to identify differences in the topography.

The topography data were also used to calculate the volume of material lost by subtracting the data from the coupons before and after exposure. The images were exported as XYZ text files for further processing into 3D data and images of the corroded surfaces (using in-house developed software). Optical 3D topography provided accurate images and 3D data of the surfaces after the removal of the oxide scale for calculating the material loss in mg/cm^2 and µm.

Dimensional Metrology

The counterparts of the coupons used for the SEM analyses were examined using Dimensional Metrology at Cranfield University. This technique generated statistical distributions of corrosion extent. The coupon dimensions were compared with the coupon thicknesses defined for each coupon with optical 3D measurements before the exposures. DM images were collected around the perimeter of the coupon cross sections. The microscope calibration allowed combining the images with x–y coordinates, enabling the measurement of the remaining thickness of the coupon and providing local information, such as any internal damage within the cross sections. The extent of change in the sample dimensions was determined by comparing the measurements with the initial thickness from the optical 3D data. DM analyses of unexposed reference coupons were used to correct for any systematic error in the measurement process. As the deposit was on the sample's top surface, a sample without a deposit was used to correct the effect of the corrosion induced without a deposit. The changes in the sample dimensions were reordered from the highest to the lowest, generating a cumulative probability distribution of change.

The damage was presented as "metal change" to identify the amount of metal corroded and as "sound metal change" for the amount of metal corrosion and internal changes, e.g., grain boundary effects. The data produced are in accordance with the standards used for high-temperature corrosion assessment [7, 8].

Results

Measured and Calculated Metal Loss

The measured and calculated mass change and metal thinning after the deposit and furnace exposures are presented in Table 3. The metal thinning was calculated using two approaches: gravimetric mass change and volume change measured with 3D profilometer. The two thinning values are also compared in Fig. 3. Figure 3 clearly emphasizes the impact of temperature on the material thinning. This was assumed to depend mainly on the presence of melt in 10K1Cl at 575 °C (Fig. 1). The trends in mass loss aligned well with the exposure temperature and the coupon alloying degree, i.e., mass loss increased with temperature, and corrosion resistance increased with chromium and nickel contents in the alloys.

The measured material loss [mg] of AISI316 exposed to 10K1Cl was around 80 times higher at 575 °C than at 500 °C. Correspondingly, the measured mass loss for AISI316 after the exposure to 1K10Cl was about 5 times higher at 575 °C than at 500 °C. It should be noted that the measured weight losses for the steels exposed to both deposits were very low at 500 °C.

Although the initial contact area of the synthetic deposit with the coupon was the same for all experiments, the surface areas showing distinct corrosion varied

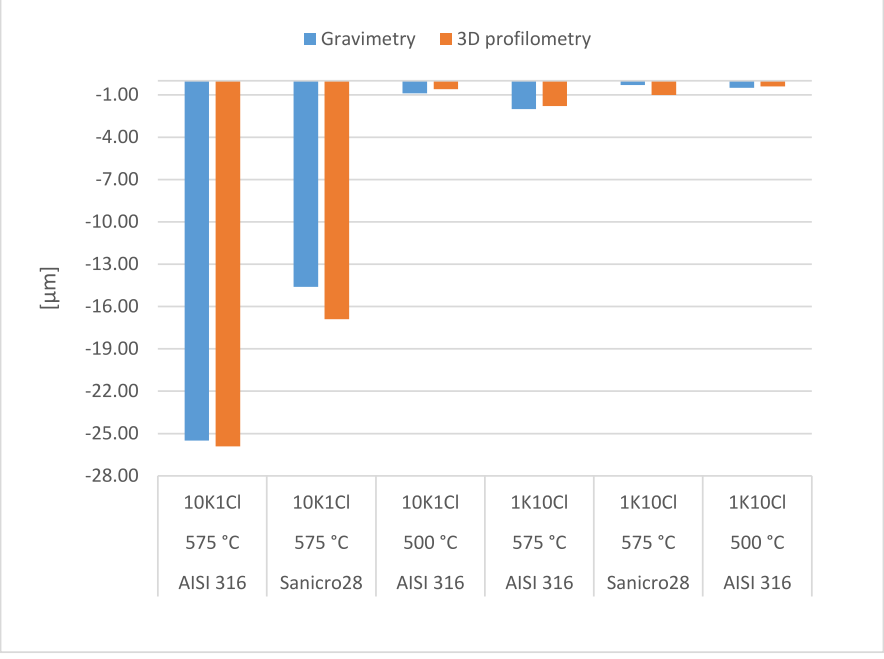


Fig. 3 Calculated material thinning values of the exposed samples. Blue columns show thinning estimations based on gravimetry and orange columns on 3D profilometer measurements

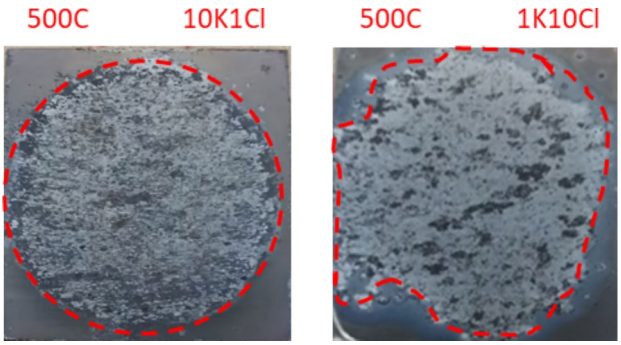


Fig. 4 Examples of visible corroded areas after removing deposit and oxide scale. The red line illustrates the area used in calculations

Table 4 Measured oxide thickness and standard deviation (SEM) and oxide thickness calculated from mass loss data for AISI316 and Sanicro28 after each exposure

Alloy	Temp	Deposit	Measured oxide thickness [µm]	Std oxide thickness [µm]	Weighed mass loss [mg]	Calculated oxide thickness [µm]
AISI316	575 °C	10K1Cl	56	24.6	134.8	56.1
AISI316	500 °C	10K1Cl	*1.1*	*2.9*	*1.7*	*1.9*
AISI316	575 °C	1K10Cl	4.9	2.2	6.7	4.4
AISI316	500 °C	1K10Cl	*1.6*	*2.5*	*1.4*	*1.0*
Sanicro28	575 °C	10K1Cl	43	16.1	49.4	32.5
Sanicro28	575 °C	1K10Cl	*1.1*	*2.8*	*1.0*	*0.7*

Values in italic are close to the detection limit.

between the samples, as shown by the images in Fig. 4. The average metal loss [mg/cm^2] in Table 3 was related to the visible corroded area measured for each coupon surface.

Measured and Estimated Oxide Scale Thickness

Oxide scale thickness was measured from the cross-sectional images using SEM (Table 4). Figure 5 shows the colored oxide scales on AISI316 exposed to the 10K1Cl and 1K10Cl deposits at 575 °C. Both samples were analyzed with the new in-house software and compared with the original manual coloring procedure [11, 14]. The new method gave lower thickness values for complex oxide scales within deposits (56 µm vs. 80 µm with AISI316, 10K1Cl at 575 °C). This was assumed to be due to a more accurate separation of the oxide scale from deposit particles. Thin, simple layers gave a minor difference (4.9 µm vs. 6.2 µm with AISI316, 1K10Cl at 575 °C).

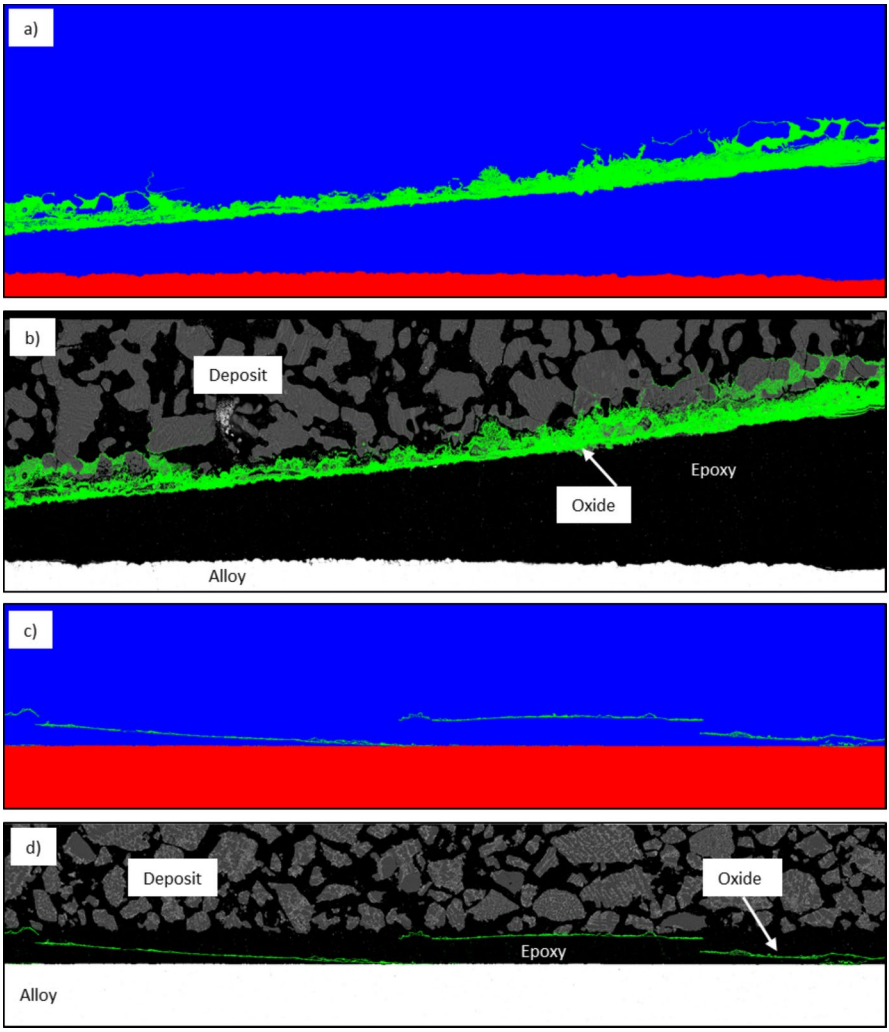


Fig. 5 SEM images of the coupon cross sections treated using two coloring methods. Images **a** and **c** show oxide scales colored manually, **b** and **d** oxide scales colored with Corrosion Analyzer software developed in this work. The green areas show the oxide scales on AISI316 exposed to 10K1Cl deposit (upper images) and 1K10Cl deposit (lower images). Both coupons had been exposed to the deposits at 575 °C

The average mass loss was used to estimate the oxide scale thickness by assuming a non-porous scale consisting of iron and chromium oxides. However, the scale morphology in the SEM images and EDX analyses indicates that the scale was porous, and its composition varied locally. When calculating the oxide scale thickness from the mass loss data, iron and chromium were assumed to form Fe_2O_3 and Cr_2O_3 in the same ratio as in the metal. Then, the densities of these oxides, 5.24 g/cm^3 for Fe_2O_3 [15] and 5.22 g/cm^3 for Cr_2O_3 [16], were used to calculate the oxide layer thickness

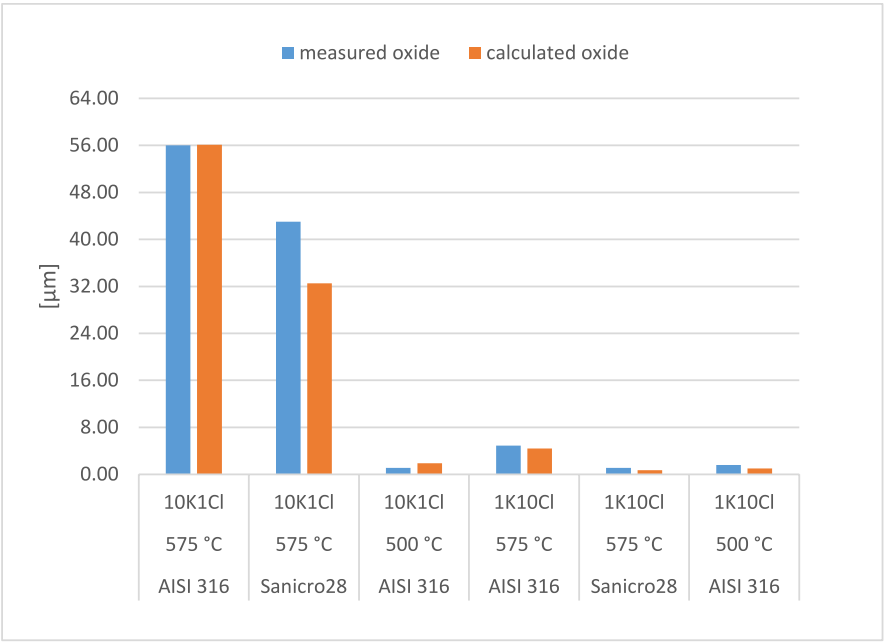


Fig. 6 Measured and calculated oxide thickness values of the exposed samples. Blue columns show measured values (SEM) and orange values estimated values from gravimetry

Table 5 Measured volume loss and projected area (3D profilometry) for AISI316 and Sanicro28 after the exposures

	10K1Cl				1K10Cl			
	500 °C		575 °C		500 °C		575 °C	
	AISI316	Sanicro28	AISI316	Sanicro28	AISI316	Sanicro28	AISI316	Sanicro28
Volume loss [mm^3]	0.25	0.20	10.40	7.09	0.18	0.16	0.76	0.42
Area [mm^2]	407.4	419.2	401.5	419.8	415.26	419.3	422.5	416.5

for the coupon area that showed visible signs of attack. Interestingly, despite several assumptions, the calculated scale thickness was comparable to the measured thickness (Table 4 and Fig. 6). The scale thickness increased with the mass loss.

Material Loss from Optical 3D Measurements

The material loss was also calculated from the 3D measurement data. The entire metal top surface area (20×20 mm^2) was measured by combining 256 images of every sample before and after exposure.

The device software used the 3D data of the coupon surfaces before and after exposure to assess the material loss volume of the projected area (Table 5). Similar to the procedure described in 3.1, the volume loss was used to calculate the material loss per surface area and metal thinning (Table 3). The calculated material thinning values based on the 3D measurements were surprisingly close to those based on the mass loss measurements (Table 3, Fig. 3).

The topography data (XYZ) were exported and treated to produce topography images of the corroded coupons, as shown for AISI316 and Sanicro28 after exposure to 10K1Cl at 575 °C (Fig. 7). The calculated thinning for these samples was of the same order (Table 3).

However, the topography images reveal differences in the corrosion patterns, suggesting deeper and more corrosion pits for AISI316 than Sanicro28.

Dimensional Metrology

The corrosion was also determined with Dimensional Metrology from the counterparts of the samples measured with SEM at Åbo Akademi. The dimensional metrology data for the deposit-exposed coupons are reported in Fig. 8.

Comparing Fig. 8a and b suggests no internal damage for AISI316. For AISI316, the main difference in the curves (8a) is due to the deposit, with 10K1Cl showing higher metal change than for 1K10Cl deposit at both studied temperatures, 500 °C and 575 °C. The median metal change (50% probability) calculated for AISI316 exposed to 10K1Cl was −55 and -60 µm at 500 °C and 575 °C, respectively. The exposure to 1K10Cl gave a median metal change of -23 µm at both temperatures. AISI316 showed a high sensitivity to the deposit composition, while the exposure temperature did not significantly affect the amount of metal change suggested by DM analysis.

Sanicro28 showed a different behavior. The sound metal change suggested internal damage in Sanicro28 (Fig. 8d). The blue curve in Fig. 8d shows high level of sound metal change for ~30% of the surface, indicating a local effect.

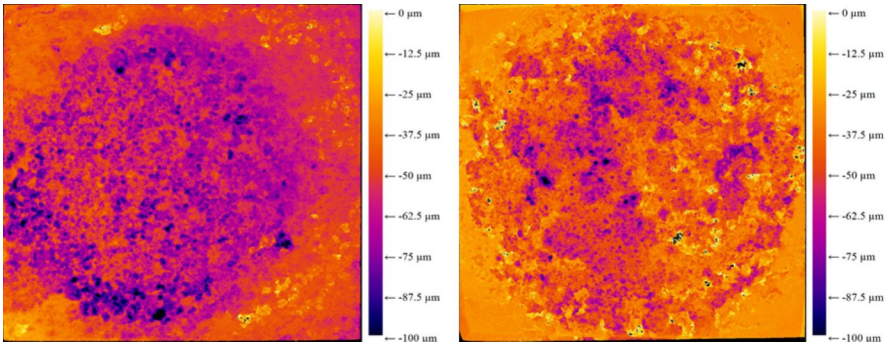


Fig. 7 Optical 3D measurement images of AISI316 and Sanicro28 samples were exposed to 10K1Cl at 575 °C

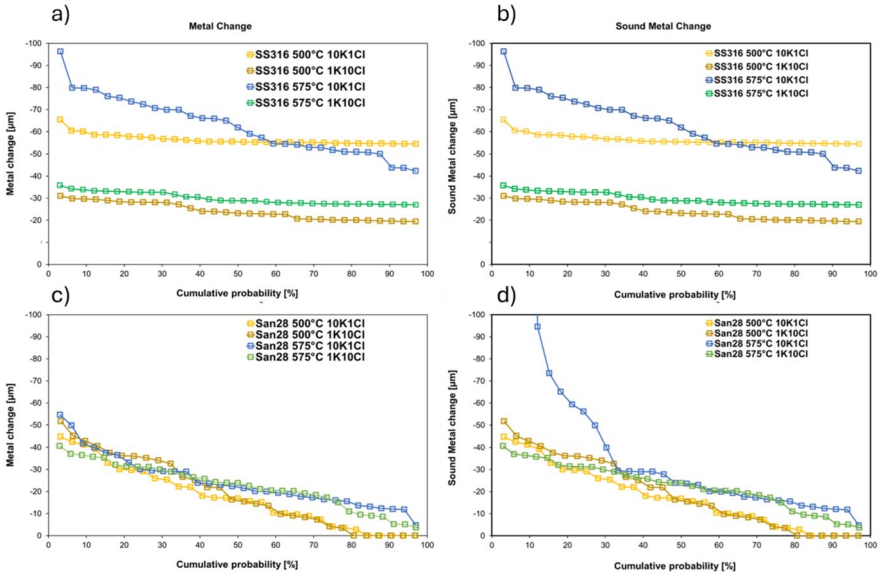


Fig. 8 Cumulative probability distribution of **a** metal change for AISI316, **b** sound metal change for AISI316, **c** metal change for Sanicro28, and **d** sound metal change for Sanicro28

The overall metal change for Sanicro28 showed higher resistance to corrosion than AISI316. The median metal change for Sanicro28 exposed to 1K10Cl was − 17 and − 22 µm at 500 °C and 575 °C, respectively. The median values were almost the same, − 16 and − 24 µm, after the exposure to 1K10Cl at 500 °C and 575 °C, indicating that the corrosion depended rather on the temperature than the deposit composition.

Oxide Scale Composition and Morphology

The oxide scales were studied using detailed SEM images and EDX analyses to understand the scale morphology and composition better. Since the reference coupons without a deposit showed negligible corrosion, their SEM images are not shown.

The thickness of the oxide scale on coupons with deposits increased with temperature and varied from a thin monoscale to a thick, porous scale. At 500 °C, minor oxidation (scale thickness 1–2 µm) was identified on the AISI316 coupons for both deposits (Fig. 10), while the oxide scale was negligible on Sanicro28 (Not shown). In contrast, more severe corrosion was identified at 575 °C, especially for the coupons exposed to 10K1Cl (Fig. 9a-d).

SEM–EDX images with a higher magnification of the thin oxide scale on AISI316 at 500 °C suggested a duplex structure consisting of an outer Fe-rich and inner Cr-rich layer for both deposits (Fig. 10a and b). Such a duplex structure has been reported to form due to the outward diffusion of iron. Simultaneously,

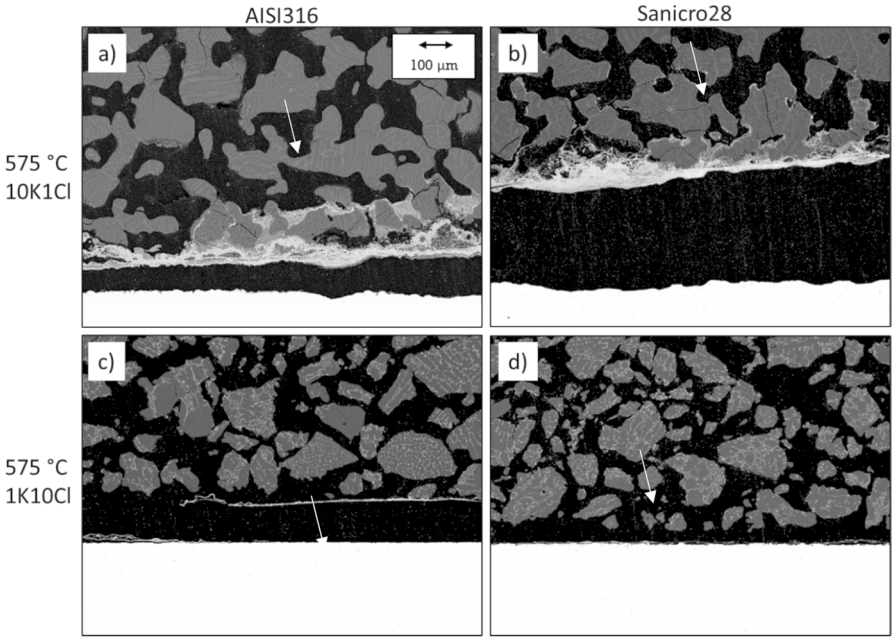


Fig. 9 Cross-sectional SEM images of the interfaces of the coupon surfaces and deposits at 575 °C **a–d**: **a** AISI316 and 10K1Cl, **b** Sanicro28 and 10K1Cl, **c** AISI316 and 1K10Cl, and **d** Sanicro28 and 1K10Cl. The magnification is the same for all images. White arrows indicate neck formation

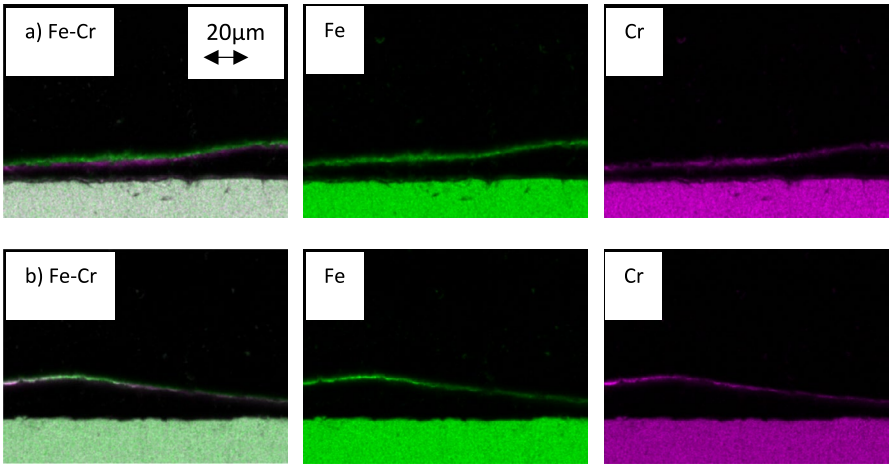


Fig. 10 Cross-sectional SEM–EDX images of AISI316 in the presence of the tested deposits at 500 °C: **a** 10K1Cl, **b** 1K10Cl

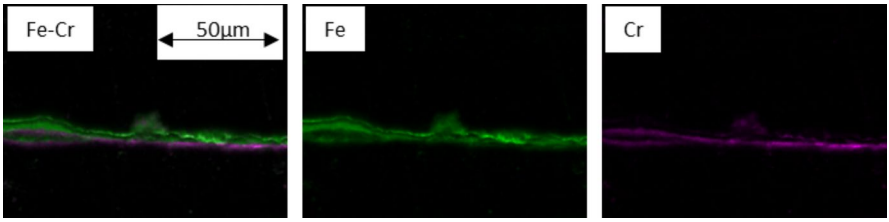


Fig. 11 SEM cross-sectional SEM images and EDX maps of Fe and Cr in the oxide layer on AISI316 after exposure to 1K10Cl at 575 °C

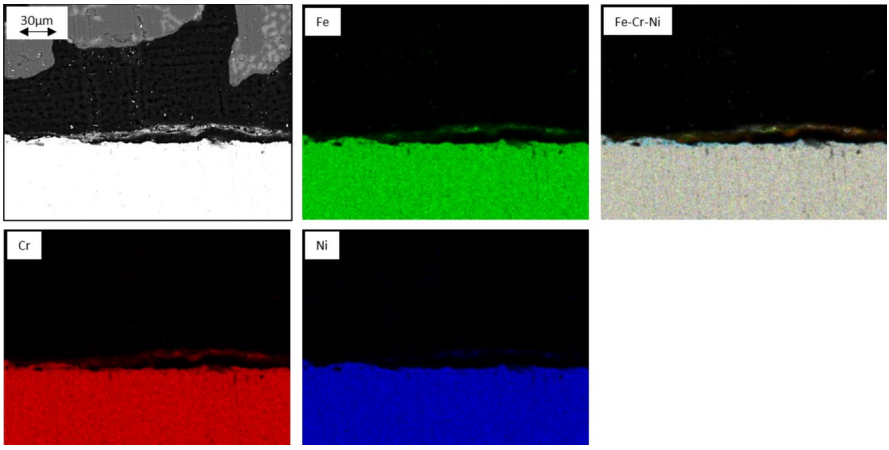


Fig. 12 Cross-sectional SEM image and EDX maps of Sanicro28 exposed to 1K10Cl at 575 °C

chromium oxidizes underneath the iron-rich oxide scale by the inward diffusion of oxygen. An accumulation of iron chloride at the scale substrate interface has been assumed to reduce the adhesion of the oxide scale, resulting in scale spallation [17]. Whether the poor adherence of the thin oxide layer in this work depends on iron chloride accumulation is unclear.

After the exposure to 10K1Cl at 575 °C, the oxide scale thickness was 56 µm on AISI316 and 43 µm on Sanicro28 (Table 4, Fig. 9a and b). In contrast, exposure to 1K10Cl at the same temperature resulted in much thinner oxide scales: 5 µm on AISI316 (Fig. 11) and approximately 2 µm on Sanicro28 (Fig. 12). Laboratory tests simulating the conditions of straw combustion and the cofiring of coal and straw revealed that an increase in potassium chloride (KCl) content led to more severe corrosion [18]. However, in the present study, a similar trend was not observed. It is essential to note that the gas atmosphere in this study differed.

SEM images of 10K1Cl salt particles, shown in Fig. 9a, b, revealed neck formation and rounded surfaces at 575 °C. This suggested partial melting of the deposit, indicating viscous flow-assisted sintering. This behavior was anticipated since the exposure temperature exceeded the deposit's first melting temperature, and the calculated melt content was around 10 wt% (Table 2, Fig. 1). Thus, the

higher corrosion induced by the salt with the lower chlorine content, 10K1Cl, was most likely caused by melt formation. Correspondingly, the much thinner oxide scales after the exposure to 1K10Cl could be explained by its first melting temperature of 613 °C (Table 2) being around 40 °C higher than the exposure temperature of 575 °C. At this temperature, the oxide scales on AISI316 and S28 exposed to 1K10Cl had duplex-structured Fe- and Cr-rich layers with slightly thicker iron oxide parts (Figs. 11, 12).

The composition and morphology of the thick (50–60 µm) oxide scale on AISI316 exposed to 10K1Cl at 575 °C are shown in Fig. 13. Interestingly, not only Fe, Cr, and Ni but also S was identified in the layer. AISI316 exposed to 10K1Cl at 575 °C also showed grain boundary corrosion (Fig. 13). Also, Sanicro28 showed marked corrosion when exposed to 10K1Cl at the higher temperature, forming a thick (40–50 µm) Fe-, Cr-, and Ni-rich layer (Fig. 14). Interestingly, chromium was also identified above the original alloy surface. Fe and Ni were analyzed around the partly molten deposit particles closest to the metal surface. Additionally, some S was identified under the oxide layer, suggesting that the deposit had partly melted during the exposure and given rise to molten salt corrosion. Although there are similarities to sulfate-induced hot corrosion, the corrosion observed in the current study occurs

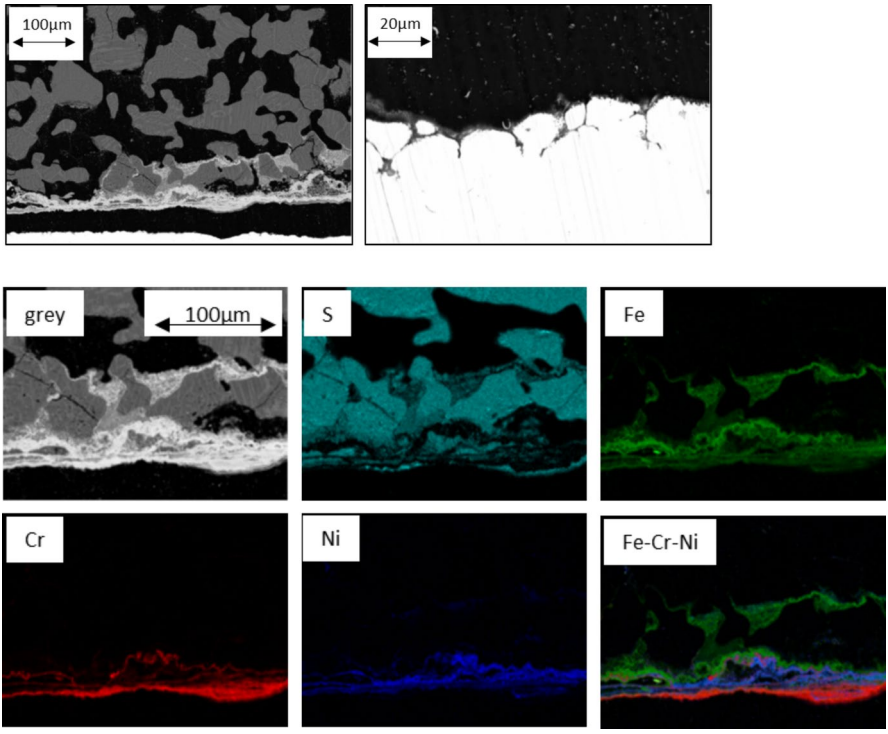


Fig. 13 SEM images (upper) and cross-sectional SEM–EDX images (lower) of AISI316 in the presence of the tested deposits at 575 °C with 10K1Cl deposit

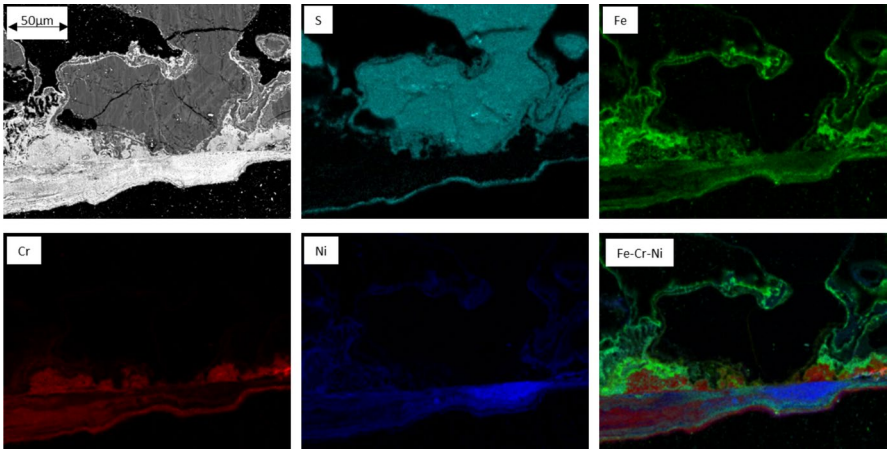


Fig. 14 Cross-sectional SEM–EDX images of Sanicro28 at 575 °C with 10K1Cl deposit

via a different reaction mechanism. Firstly, the applied temperatures are well below the ones reported for hot corrosion [19]. Secondly, hot corrosion is often reported to require the presence of SO_3 to stabilize the sulfates [20].

Discussion

The oxidation rates of steels have been evaluated qualitatively, by measuring the sample's mass change [21] or the thickening of the oxide layer [22]. The thickness of the oxide layer correlates with the mass loss of the steel [23]. According to Nielsen et al. [22], the corrosion rate of iron- and chromium-based alloys follows the parabolic law. However, the temperature and composition affect the details of the time-dependent corrosion of different steels [24–29]. In general, the rate of corrosion increases with increasing temperature, but again, the magnitude of the change depends on the composition of the steel [24, 26, 28–32].

The corrosion behavior of steel can change dramatically depending on temperature, even at temperatures below the melting point of the deposit. The temperature affects the magnitude of corrosion and the type of degradation, e.g., metal loss, irregularities at the oxide/metal interface, and the depth of internal attack [32].

As expected, Sanicro28, with a higher chromium content, formed a thinner corrosion product layer than AISI316, thus verifying its better corrosion resistance (Fig. 9 and Table 4). For steel, to maintain the protective oxide layer, the diffusion of chromium from the bulk metal must occur at a sufficient rate to balance the rate at which chromium in the protective layer is consumed to form the corrosion oxide scale [33]. The temperature-dependent diffusion of chromium takes place mainly along the grain boundaries.

Sulfur in the layer next to the metal surface for AISI316 and Sanicro28 after 10K1Cl at 575 °C suggested that the partly molten deposit resulted in accelerated

corrosion. Although the results resemble the hot corrosion phenomenon, the temperature during the exposure, 575 °C, was much lower than the temperatures usually reported for type II hot corrosion [19]. Type II hot corrosion, sometimes called low-temperature hot corrosion, occurs between 600 and 750 °C and involves the formation of a molten eutectic mixture of Na_2SO_4 and MSO_4 that requires a certain concentration of sulfur trioxide for stabilization [20]. If these sulfates are present, they can react with alkali metals, creating low-melting-point salts that impede protective oxide layer formation [19]. As the temperature in this work exceeded the first melt temperature of 10K1Cl, resulting in around 10 wt% melt, it was assumed that the corrosion mechanism was similar to low-temperature hot corrosion caused by molten salt. The impact of melt formation on corrosion is apparent for the salt with the lower Cl content (10K1Cl), as demonstrated by the increases in mass loss (Table 3), oxide thickness (Table 4), and volume loss (Table 5) above the first melting temperature of the salt.

The first melting temperatures (Table 2, Fig. 1) were calculated for the system K-Na-Cl-SO_4 using the nominal and analyzed salt compositions. However, if $FeCl_2$ or some other compound formed in the reactions between the alloy and the halide chlorides, the T_0 of the deposit was likely lower. Thermodynamic calculations [34] have suggested that a minor amount of $FeCl_2$ in a KCl deposit gives melt formation at temperatures as low as 500 °C. Additionally, molten sodium sulfate is believed to initiate corrosion [35]. In this work, the amount of the molten phase, around 10 wt%, in the scale on the alloys during the exposure to 10KCl1 at 575 °C was assumed to be enough to induce significant corrosion. The thick corrosion layer, deposit morphology, and calculated melt formation in the deposit emphasized the need for a detailed understanding of the melt formation in the scales.

Various instrumental methods were used to characterize phenomena that had occurred on the two alloys, AISI316 and Sanicro28, after exposure to potassium- and chlorine-containing synthetic salts. These methods provided different approaches to directly or indirectly explain corrosion. Table 6 summarizes the outcome of each method and technique, highlighting their main advantages and disadvantages. Each instrumental method had unique outcomes, benefits, and disadvantages. This work aimed to compare those and help choose the proper method or methods for the task.

As the table shows, none of the tested methods provided information to all relevant features, i.e., they were not all-inclusive, and choosing the proper method depends on the information needed.

The thickness of the corrosion scale calculated from the mass of the corroded steel agreed well with the thickness measured in the interfacial area of the deposit and alloy surface provided by SEM panorama images (Table 4 and Fig. 6). A new procedure to define the oxide scale thickness in SEM images was developed. Compared to the old coloring method [9, 12], the new procedure provided an easier and faster measurement of the scale thickness. Moreover, the new procedure was based on automated image analysis, thus minimizing errors from visual selection of the area to be colored and measured.

All the methods required sample treatment prior to and after exposure. 3D optical measurement of a surface from which the scale had been removed provided detailed information about local attacks. Details in 3D images gave information

Table 6 Outcome, benefits, and disadvantages of instrumental methods used to characterize steel surfaces after laboratory exposures to corrosive salt deposits

Method	Outcome	Advantages	Disadvantages
Mass loss, combined with visual inspection	Calculated material loss [mg], [mg/cm^2], or [µm]	Straightforward method, cheap, provides average mass loss	Requires the removal of the oxide scale and thus fails to give detailed information on the corrosion mechanisms
3D measurement for a surface from which corrosion layers removed	Topography images and profiles, calculated material loss [mg/cm^2] or [µm] for an alloy with known density	Visualization of corroded surfaces in 3D, enables the identification of local phenomena, e.g., corrosion pits	Work-intensive measurement, chemical information lost in sample preparation
Dimensional Metrology for a cross section of the alloy after exposure	Statistical probability of material degradation, median material loss [µm]	Deposit not removed, which enables EDX analyses. Provides information on material loss from surfaces but also on phenomena along grain boundaries	Sample preparation and measurement are laborious; requires a reliable definition of the sample dimensions before exposure
SEM + EDX of the metal surface and cross section of metal surface–deposit interface	High-magnification images, oxide (i.e., corrosion) scale thickness, structure, and composition	Detailed information on the morphology and composition of metal surfaces	Sample preparation and measurement are laborious, expensive

about the corrosion features that were not revealed by the numbers describing the surface topography. These images showed differences in the material loss patterns, thus suggesting whether the corrosion was uniform or had pitting-like features. As the 3D optical measurement only provides topography data and was done for a surface from which the deposit and oxide layer had been removed, all information related to the composition and morphology of the oxide layer and deposit was lost. The 3D method was quite time and effort intensive. Interestingly, material thinning calculated from 3D measurements and weight loss measurements were comparable, thus suggesting weight loss as a more straightforward alternative if detailed information of the topography features is not needed.

Most metal corrosion measured using DM suggested more severe corrosion than the other methods, but the trends were similar. This difference was assumed to be due to different factors, the most significant being that the initial thickness measured with the profilometer was used as the initial value for DM thickness analyses. Comparing the initial thickness with detailed values measured for the total cross section using SEM suggested that thickness values derived from profilometer measurements had a systematic error of around 50 µm. First, the profilometer did not account for any topography differences on the downside of the coupons. Second, although sensitive to minor topography variations, the average coupon thickness, 5 mm, was too large to measure the overall coupon thickness. Thus, the differences between the corrosion depth as suggested by the metal change values of DM and calculated thinning values (from weight change and 3D measurements) were assumed to mainly depend on inaccurate values for the metal before the treatments.

Local degradation of the Sanicro28 alloy at 575 °C due to internal attack could be verified by the sound metal change probability (Fig. 8d) but not with SEM measurements (Fig. 14). On the other hand, metal change values indicated corrosion within some surfaces that did not show similar signs of corrosion according to the weight measurements or detailed SEM images (AISI316, 10K1Cl, 500 °C in Fig. 8a and Fig. 9a). Magnified SEM images were taken to verify whether local corrosion attacks had taken place in the samples for which the sound metal change was exceptionally high for some points. The SEM images suggested that other substances (e.g., residuals from polishing) had attached to the metal surface (Fig. 15). It was assumed that DM identified these substances as deviations in the metal surface, contributing to sound metal change values. Again, when analyzing the oxide layer thickness using SEM–EDX and the new software, areas of different compositions were neglected. Surface pretreatments for the analyses appeared to be critical. Thus, identifying intact metal and corrosion products from other substances (e.g., dirt from polishing) is more accurate with SEM than with a microscope based on visual light. Examples of these leftovers are shown in Fig. 15.

Furthermore, the DM images were taken at a magnification of 20X, while the SEM had a much higher magnification (100X). Thus, different equipment-specific factors most likely affected the measured and calculated values of the oxide layer, deposit, and intact metal.

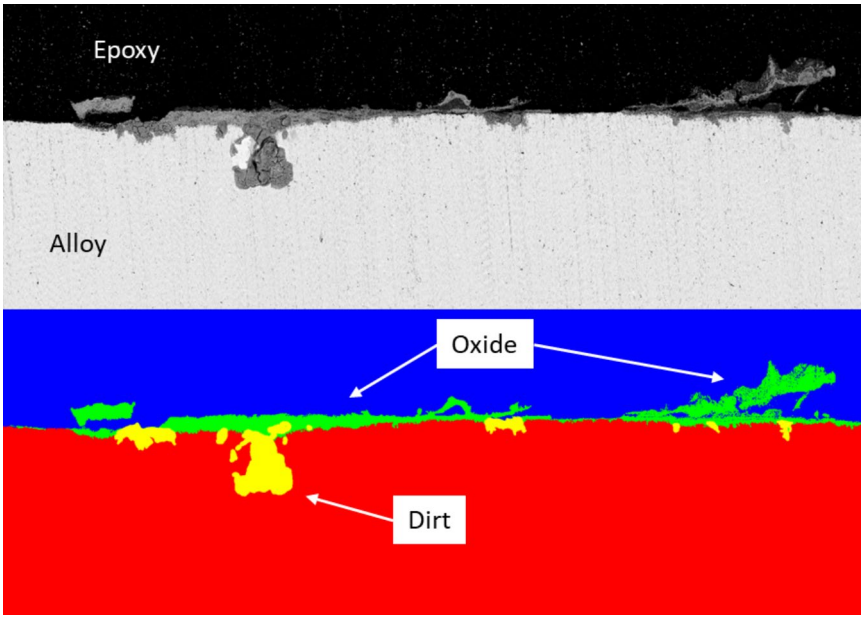


Fig. 15 Example of dirt in SEM images (Sanicro28, 10K1Cl, 575 °C) after surface polishing. The oxide scale is shown in green and dirt in yellow

Conclusions

This study compared various instrumental methods for identifying and calculating material thinning in AISI316 and Sanicro28 steels due to exposure to two synthetic deposit mixtures composed of Na_2SO_4, K_2SO_4, NaCl, and KCl, close to their first melting temperatures. Additionally, the thickness, morphology, and composition of the oxide scales formed on the steels were analyzed.

The use of composition-dependent brightness ranges in the SEM micrographs facilitated a quicker process for determining the thickness and composition of the oxide scales. By applying different colors to represent various brightness levels, it became possible to automatically calculate the average thickness for each oxide associated with a specific color.

Oxide scale thicknesses measured using dimensional metrology were sensitive to the specification of the initial sample dimensions. Thus, any inaccuracies in the starting values led to significant deviations from the results obtained using other methods.

The measured mass loss and the values derived through volume losses gave comparable results. However, mass loss is a more straightforward procedure. Notably, calculating the oxide scale thickness from mass loss provided values very close to those measured with SEM.

The results confirmed that the presence of melt in the deposit has a significant impact on metal corrosion. In general, deposits with high chlorine content are critical for initiating corrosion. In this work, a deposit containing 10wt% chlorine

without any molten phase was less corrosive than one with just 1wt% chlorine but with 10wt% melt at the exposure temperature. Consequently, even a small amount of chlorine can trigger corrosion when a partially molten deposit is present.

Scale thickness helps compare the performance of different alloys in a specific environment. However, for a detailed understanding of the corrosion mechanisms, SEM–EDX analyses are essential. In contrast, average corrosion can be easily characterized by measuring the change in mass.

Author Contributions Jan-Erik Eriksson: Conceptualization, Methodology, Analyses, Writing—original draft, In-House Software design. Juho Lehmusto: Conceptualization, Methodology, Analyses, Writing—original draft, Writing—review and editing, Supervision, Project administration, Funding acquisition. Stefano Mori: Methodology, Dimensional Metrology, Writing—original draft. Linus Silvander: SEM operator, 3D operator, In-House software developer. Leena Hupa: Funding acquisition, Writing—original draft, Writing—review and editing.

Funding Open access funding provided by Åbo Akademi University. This work was conducted within the Academy of Finland project "Initiation and propagation of high-temperature corrosion reactions in complex oxygen-containing environments" (Decision no. 348963). The research was also part of the activities of the project Clean and efficient utilization of demanding fuels (CLUE2023-2025) supported by the industrial partners: ANDRITZ Oy, Valmet Technologies Oy, UPM-Kymmene Oyj, Metsä Fibre Oy, and International Paper Inc.

Data Availability No datasets were generated or analysed during the current study.

Declarations

Conflict of interest The authors declare no competing interests.

Open Access This article is licensed under a Creative Commons Attribution 4.0 International License, which permits use, sharing, adaptation, distribution and reproduction in any medium or format, as long as you give appropriate credit to the original author(s) and the source, provide a link to the Creative Commons licence, and indicate if changes were made. The images or other third party material in this article are included in the article's Creative Commons licence, unless indicated otherwise in a credit line to the material. If material is not included in the article's Creative Commons licence and your intended use is not permitted by statutory regulation or exceeds the permitted use, you will need to obtain permission directly from the copyright holder. To view a copy of this licence, visit http://creativecommons.org/licenses/by/4.0/.

References

1. T. L. S. van Loo, J. Koppejan, *UPDATE*, 4, (2008).
2. UN DESA. The Sustainable Development Goals Report 2024—June 2024. New York, USA: UN DESA. © UN DESA, 2024. https://unstats.un.org/sdgs/report/2024/.
3. J. M. Brossard, I. Diop, X. Chaucherie, F. Nicol, C. Rapin, and M. Vilasi, *Materials and Corrosion* **62**, 543 (2011).
4. S. Enestam, *Corrosivity of hot flue gases in the fluidized bed combustion of recovered waste wood*, PhD Thesis (Åbo Akademi University, 2011).
5. Z. Yan, L. Wang, X. Li, J. Wei, C. Liu, and Y. Da, *Engineering Failure Analysis* **139**, 106457 (2022).
6. High Temperature Corrosion: Fundamentals and Engineering, César A. C. Sequeira (ISBN: 978-1-119-47444-9, 656, 2018).

7. BSI Standards, *Corrosion of Metals and Alloys—Guidelines for Applying Statistics to Analysis of Corrosion Data* (BS ISO 14802:2012).
8. N. J. Simms et al., *Lifetime Modelling of High Temperature Corrosion Processes* (EFC No. 34, p. 246 [ed. Schütze M, et al], Maney, 2001).
9. S. Mori, A. Pidcock, J. Sumner, N. Simms, and J. Oakey, *Oxidation of Metals* **97**, 281 (2022).
10. J.-E. Eriksson, J. Lehmusto, M. J. Dirbeba, L. Silvander, D. Lindberg, and L. Hupa, *Fuel* **348**, 128516 (2023). https://doi.org/10.1016/j.fuel.2023.128516.
11. B.-J. Skrifvars, R. Backman, M. Hupa, K. Salmenoja, and E. Vakkilainen, *Corrosion Science* **50**, 1274 (2008).
12. D. Bankiewicz, *Corrosion behaviour of boiler tube materials during combustion of fuels containing Zn and Pb*. Doctoral thesis (Turku, Finland: Åbo Akademi University, 2012).
13. R. Balint, M. Engblom, J. Niemi, M. Hupa, and L. Hupa, *Fuel* **359**, 130386 (2024).
14. M. Westén-Karlsson, *Assessment of a laboratory method for studying high temperature corrosion caused by alkali salts* (Åbo Akademi University, 2008).
15. Iron oxide (Fe2O3). CAS Common Chemistry. CAS, a division of the American Chemical Society, n.d. (CAS RN: 1309-37-1). Licensed under the Attribution-Noncommercial 4.0 International License (CC BY-NC 4.0).
16. Chromia. CAS Common Chemistry. CAS, a division of the American Chemical Society, n.d. (CAS RN: 1308-38-9). Licensed under the Attribution-Noncommercial 4.0 International License (CC BY-NC 4.0).
17. T. Jonsson, N. Folkeson, J.-E. Svensson, L.-G. Johansson, and M. Halvarsson, *Corrosion Science* **53**, 2233 (2011).
18. S. C. V. Lith, F. J. Frandsen, M. Montgomery, T. Vilhelmsen, and S. A. Jensen, *Energy & Fuels* **23**, 3457 (2009).
19. F. Pettit, *Oxidation of Metals* **76**, 1 (2011).
20. L. F. Aprigliano, *Burner Rig Simulation of Low Temperature Hot Corrosion*. David W. Taylor Naval Ship Research and Development Center (Report MAT-77-68, 1977).
21. J. Pettersson, H. Asteman, J.-E. Svensson, and L.-G. Johansson, *Oxidation of Metals* **64**, 23 (2005).
22. H. P. Nielsen, F. J. Frandsen, and K. Dam-Johansen, *Energy & Fuels* **13**, 1114 (1999).
23. S. C. Cha, *Corrosion Engineering, Science and Technology* **42**, 50 (2007).
24. H. J. Grabke, E. Reese, and M. Spiegel, *Corrosion Science* **37**, 1023 (1995).
25. M. Spiegel, *Materials and Corrosion* **50**, 373 (1999).
26. M. Sánchez-Pastén and M. Spiegel, *Materials and Corrosion* **57**, 192 (2006).
27. Y. Shinata and Y. Nishi, *Oxidation of Metals* **26**, 201 (1986).
28. A. Zahs, M. Spiegel, and H. Grabke, *Corrosion Science* **42**, 1093 (2000).
29. J. Pettersson, J.-E. Svensson, and L.-G. Johansson, *Oxidation of Metals* **72**, 159 (2009).
30. Y. Shinata, *Oxidation of Metals* **27**, 315 (1987).
31. N. Folkeson, T. Jonsson, M. Halvarsson, L.-G. Johansson, and J.-E. Svensson, *Materials and Corrosion* **62**, 606 (2011).
32. K. Weulersse-Mouturat, G. Moulin, P. Billard, and G. Pierotti, *Materials Science Forum* **461–464**, 973 (2004).
33. N. K. Othman, J. Zhang, and D. J. Young, *Materials and Corrosion* **62**, 496 (2011).
34. J. E. Eriksson, J. Lehmusto, L. Silvander, D. Lindberg, M. Zevenhoven, P. Yrjas, and L. Hupa, *High Temperature Corrosion of Materials* **101**, 123 (2024).
35. G. Y. Lai, *High Temperature Corrosion of Engineering Alloys*, (ASM International Book, 1990), p. 15.

Publisher's Note Springer Nature remains neutral with regard to jurisdictional claims in published maps and institutional affiliations.



https://dspace.org/

Comparison of laboratory-scale methods for assessing deposit-induced corrosion of boiler materials in biomass combustion and recovery boilers

Eriksson, Jan-Erik; Mori, Stefano; Silvander, Linus; Hupa, Leena; Lehmusto, Juho

2025-08-01
Springer
https://doi.org/10.1007/s11085-025-10339-1
Eriksson J-E, Mori S, Silvander L, et al., (2025) Comparison of laboratory-scale methods for assessing deposit-induced corrosion of boiler materials in biomass combustion and recovery boilers. High Temperature Corrosion of Materials, Volume 102, Issue 4, August 2025, Article number 19

Downloaded from a DSpace repository. https://dspace.org/